Reactive transport modelling of the long-term interactions of corrosion products and compacted bentonite in a HLW repository in granite: Uncertainties and relevance for performance assessment

Javier Samper, Acacia Naves, Luis Montenegro, Alba Mon

University of A Coruña, 15071 La Coruña, Spain, jsamper@udc.es

Abstract. Here we present a long-term nonisothermal reactive transport model for the interactions of the corrosion products of a carbon-steel canister and the compacted bentonite of the engineered barrier of a high-level radioactive waste repository in granite. Canister corrosion causes an increase in the pH and the concentration of dissolved Fe^{2+} of the bentonite porewater. Iron precipitates as magnetite and siderite and sorbs via cation exchange and surface complexation on weak sites. Magnetite precipitation reduces significantly the porosity of the bentonite near the canister. The thickness of the zone of reduced porosity is 7 cm at t = 1 Ma. This thickness increases significantly when the dependence of the corrosion rate on the chemical conditions is considered and decreases 3 cm when smectite dissolution and analcime precipitation are taken into account. Model results are not significantly sensitive to the thermal transient and the effect of temperature on the corrosion rate. The conclusions of our simulations are consistent for the most part with those reported by other numerical analyses of the interactions of corrosion products and compacted bentonite in engineered barrier systems at similar chemical conditions.

Key words. Radioactive waste, reactive transport, corrosion products, compacted bentonite

1. Introduction

Carbon steel and compacted bentonite have been proposed as candidate materials for the overpack and buffer, respectively, in the multi-barrier system of deep geological repositories for high-level radioactive waste (HLW). The corrosion of the carbon steel may induce buffer alterations which could result in changes in parameters such as porosity, permeability, sorption and swelling. The prediction of the long-term evolution of the engineered barrier in a repository should not be a blind extension of the models developed for experiments to different space and time scales. It requires a careful assessment of the key long-term processes and their couplings as well as an evaluation of the resulting uncertainty and its consequences. Contrary to thermal, hydrodynamic and mechanical processes which will last for several hundreds to 1000 years, the geochemical reactions induced by canister corrosion will take place at all temporal scales.

Iron-bentonite interactions and the effects of corrosion products on the bentonite were first identified by NAGRA in the mid 1980's (Savage, 2012). Various experiments and modelling studies were performed by ANDRA and JAEA in the late 1990's. Some of these studies were performed by using 1D coupled thermo-hydro-chemical models (Montes-H *et al.,* 2005; Bildstein *et al.,* 2006; Wersin *et al.,* 2007; Samper *et al.,* 2008a; Savage *et al.,* 2010a; Marty *et al.,* 2010a; Lu *et al.,* 2011, Ngo *et al.,* 2014). Some models

assume that magnetite is the main product (Samper *et al.*, 2008a; Lu *et al.*, 2011) while others assume the formation of Fe-bearing aluminosilicates (Wersin *et al.*, 2007; Savage *et al.*, 2010a; Marty *et al.*, 2010a; Ngo *et al.*, 2014). Bildstein *et al.* (2006) modelled the interactions of a carbon-steel canister with the MX-80 bentonite and the clay formation in the French reference system at 50 ºC over 10.000 years. They considered the following corrosion products: iron oxides and hydroxides, iron carbonates, and iron-rich smectite and Fe-phyllosilicates. Wersin *et al.* (2007) studied the impact of iron components released from the canister corrosion on the bentonite buffer (MX-80) within the KBS-3H concept using the Olkiluoto site in Finland. They accounted for iron corrosion, cation exchange, protonation/deprotonation, Fe(II) surface complexation and thermodynamic and kinetic mineral dissolution/precipitation. Samper et al. (2008a) presented 1-D and 2-D multicomponent reactive transport models to simulate the interactions of corrosion products with bentonite in the near field of a repository in granite. Numerical simulations were performed at a constant temperature of 25 ºC for 0.3 Ma. They found that magnetite is the main corrosion product. Magnetite precipitation reduces the bentonite porosity. Lu et al. (2011) presented an updated version of the model of Samper et al. (2008a) which considers 3 types of sorption sites in the bentonite, kinetically-controlled canister corrosion and magnetite precipitation, and the competition of Ni^{2+} for sorbing sites. Savage *et al.* (2010a) reported a model of the iron-bentonite interactions based on natural analogues. They claim that the sequence of the alteration of the clay by Fe-rich fluids may proceed via an Ostwald step sequence. They modelled iron corrosion and the alteration of the MX-80 bentonite. Savage *et al.* (2010b) found that smectite dissolution may be significant for the future geochemical state of a buffer, but the time scale of this process

is too long for experimental verification. Marty *et al.* (2010a) modelled the long-term alteration of the engineered bentonite barrier in an underground radioactive waste repository. Their study focused on the feedback effects of geochemical reactions on the transport parameters of compacted MX-80 bentonite. Their calculations assumed a constant temperature of 100 ºC to estimate the maximum thermal effect on the mineralogy of the engineered barrier. The model was run for 10^5 years. Ngo et al. (2014) presented a coupled transport-reaction model for the long-term interactions of iron, bentonite and Callovo-Oxfordian (COX) claystone which extended the work of Marty et al. (2010a) by investigating the influence of the reactive surface area of the primary minerals on the bentonite and the COX claystone and the diffusion coefficient on the evolution of the iron-bentonite system.

The anoxic corrosion of the steel canister leads to the generation and accumulation of H_2 which may be present in a gaseous phase as $H_{2(g)}$ or may dissolve as $H_{2(aq)}$. As indicated by Ortiz et al. (2002), the diffusive transport of H_2 may be too slow compared to the gas generation rate, a gas phase could form and gas pressure may build up in the repository. Xu et al. (2008) reported a two-phase flow model to study H_2 gas generation, pressure buildup and saturation distribution in a nuclear waste repository. The model accounts for canister corrosion and reactive transport by using the TOUGREACT simulator. Their results show that the gas—pressure buildup depends strongly on the corrosion rate and the surface area of the canister contacted by water. They pointed out the need to determine the specific controls on the corrosion rate.

Here, we present a nonisothermal multicomponent reactive transport model to study the long-term interactions of corrosion products and compacted bentonite in a HLW repository in granite. The numerical model is then used to analyse the relevance of smectite dissolution in the long-term geochemical evolution of the bentonite barrier, evaluate the thermal transient and its effect on the corrosion rate, compare the results obtained with local equilibrium and kinetic magnetite precipitation, and compare several corrosion rate models (constant versus kinetically-controlled). The paper starts by describing the reference repository concept. Then, the reactive transport model is presented. Afterwards, the model results for the reference run are discussed. The results of the sensitivity runs are also presented. Next, the results of our model are compared to those reported by others for similar clay barriers.

2. Reference concept

The geometry of the model corresponds with the Spanish reference concept of a high level radioactive waste repository in granite (ENRESA, 2000). It consists on the disposal of spent fuel elements in cylindrical carbon steel canisters placed in horizontal disposal drifts. The disposal drifts, having 500 m in length and 2.4 m in diameter, are located at a depth of 500 m in a granite formation. The canisters are spaced 2 m. The distance between disposal drifts is 35 m. The canisters are 4.54 m long, 0.10 m thick and have an external diameter of 0.90 m. They are surrounded by blocks of compacted bentonite. The average dry density of the bentonite barrier is 1,600 kg/m^3.

3. Reactive transport model

3.1 Conceptual model

Although the blocks are initially unsaturated, the model assumes that the bentonite is initially water-saturated because the bentonite barrier will become fully saturated in less than 50 years (Zheng and Samper, 2008). The reference run starts once the thermal pulse has dissipated. Therefore, the reference run is isothermal with a constant temperature of 25ºC. Some sensitivity runs account for the nonisothermal conditions.

The hydraulic conductivity of the bentonite is extremely low ($6 \cdot 10^{-14}$ m/s). Therefore, advection is negligible and solute diffusion is the main solute transport mechanism. All the water is assumed to be accessible to solutes. Solute transport through the granite is simulated with a prescribed water flux parallel to the axis of the gallery which flushes the bentonite/granite interface (Fig. 1).

The geochemical model accounts for canister corrosion, aqueous complexation, acid/base and redox reactions, mineral dissolution/precipitation, surface complexation of Fe^{2+} and H^+ on three types of sorption sites and cation exchange reactions of Ca^{2+}, Mg^{2+}, Na^+, K^+ and Fe^{2+}. The chemical system is defined in terms of the following primary species: H_2O, $O_2(aq)$, H^+, Na^+, K^+, Ca^{2+}, Mg^{2+}, Fe^{2+}, Al^{3+}, HCO_3^-, Cl^-, SO_4^{2-} and $SiO_2(aq)$. The following aqueous complexes were identified from speciation runs performed with EQ3/6 (Wolery, 1992): OH^-, CO_3^{2-}, $CaCO_3(aq)$, $CaSO_4(aq)$, $CaOH^+$, $MgCO_3(aq)$, $MgHCO_3^+$, $MgSO_4(aq)$, $MgOH^+$, NaOH, $NaCO_3^-$, $NaHCO_3(aq)$, $CO_2(aq)$, HS^-, Fe^{3+}, $FeHCO_3^+$, $FeCO_3(aq)$, $FeCl^+$, $FeCl^{2+}$, $FeOH^+$, $FeOH^{2+}$, $Fe(OH)_2(aq)$, $Fe(OH)_3(aq)$, $Fe(OH)_4^-$, $Fe(OH)_2^+$, $Fe(SO_4)_2^-$, $FeSO_4(aq)$, $FeHSO_4^{2+}$, $Fe_2(OH)_2^{4+}$, $KOH(aq)$, KSO_4^-, $NaSO_4^-$,

HSO_4^-, $H_2(aq)$, $Al(OH)_2^+$, $Al(OH)_3(aq)$, $Al(OH)_4^-$, $Al(OH)^{2+}$, $NaH_3SiO_4(aq)$ and $H_6(H_2SiO_4)_4^{2-}$. $Al(OH)_4^-$ was used as primary species instead of Al^{3+} in the final runs. The Gaines-Thomas convention was used for cation exchange reactions. Surface complexation reactions are modelled with a triple-site model (Bradbury and Baeyens, 1997; 2005). Chemical reactions and their equilibrium constants at 25 ºC for mineral dissolution/precipitation as well as selectivity coefficients for exchanged cations and protolysis constants for surface complexation are listed in Table 1.

The available oxygen in the repository will be consumed soon after its closure, and anaerobic conditions will prevail in the long term. The canister was treated as a porous material made of 100% metallic iron, Fe(s), which corrodes according to:

$$Fe(s) + 2H_2O \rightleftarrows Fe^{2+} + 2OH^- + H_2(g) \quad (1)$$

By rewriting this reaction in terms of the primary species used in the numerical model, one obtains:

$$Fe(s) + 2H^+ + 0.5O_2(aq) \rightleftarrows Fe^{2+} + H_2O \quad (2)$$

All the reactions, except for canister corrosion, are assumed at chemical equilibrium in the reference run. Kinetically-controlled mineral dissolution/precipitation reactions were considered in the sensitivity runs. The following kinetic rate law was used for kinetic mineral dissolution/precipitation:

$$r_m = k_m e^{-\frac{Ea}{RT}} \left(\Omega_m^\theta - 1\right)^\eta \quad (3)$$

where r_m is the dissolution/precipitation rate (mol/m^2/s); k_m is the kinetic rate constant (mol/m^2/s) at 25ºC, Ea is the activation energy, R is the gas constant, T is the temperature (K), Ω_m is the saturation index which is equal to the ratio between the ion activity product and the equilibrium constant (dimensionless), and Θ and η are empirical parameters of the kinetic law.

The corrosion rate, r_c, in μm/year is calculated as:

$$r_c = \frac{r_m M_w}{\rho} \tag{4}$$

where ρ is the density of the carbon steel (7860 kg/m3), M_w is its molecular weight (55.85 g/mol) and r_m is the corrosion rate per unit mineral surface (mol/m^2/year). A constant corrosion rate of 2 μm/year, which amounts to 0.281 mol/m^2/year, was used for the reference run. It should be noticed that η = 0 for constant canister corrosion.

Smectite dissolution was simulated by assuming the chemical formulation of the FEBEX-montmorillonite derived by Fernández *et al.* (2009) (Table 1). The initial volume fraction of smectite (0.57) is equal to the total mineral volume minus the volume of quartz and calcite. The following kinetic law of Rozalén *et al.* (2008) was used to model the kinetic smectite dissolution:

$$r_m = 10^{-14.37} + 10^{-12.30}\left[H^+\right]^{0.40} + 10^{-13.05}\left[OH^-\right]^{0.27} \tag{5}$$

where $[H^+]$ is the proton activity and $[OH^-]$ is the hydroxyl activity. The smectite reactive surface area is equal to 1 m^2/L and the molar volume is equal to 134.88 cm^3/mol (Fernández *et al.*, 2009).

The Al^{3+} released by smectite dissolution may precipitate as analcime (Marty et al., 2010b; Savage, 2012). The log K of analcime at 25º C is listed in Table 1 (Savage *et al.*,

2010a; Wilkin and Barnes, 1998). The analcime kinetic precipitation rate is given by Eq. (3) with k_m = 1.26·10^{-14} mol/m^2/s, η = 1 and θ = 1 (Savage *et al.*, 2010a). The analcime reactive surface area is equal to 0.01 m^2/L and the molar volume is equal to 97.1 cm^3/mol (Fernández *et al.*, 2009). Cronstedtite precipitation is assumed at equilibrium. Its log K at 25 ºC is listed in Table 1 (Savage *et al.*, 2010a).

As pointed by Ortiz et al. (2002), we assume in our model that $H_{2(g)}$ will migrate through a cyclic opening and closure of discrete preferential pathways. Therefore, $H_{2(g)}$ migration is neglected and only the diffusion of $H_{2(aq)}$ is accounted for in our model.

3.2 Numerical model

A 1-D axisymmetric numerical model of the canister and the bentonite was used to simulate the long term interactions of the corrosion products and the bentonite (Fig. 1). Water flow and solute transport through the granite was simulated with a constant water flux of 0.1 L/y parallel to the axis of the gallery at the bentonite-granite interface. The finite element mesh has 93 nodes and 92 elements. Numerical simulations were performed for a time horizon of 1 Ma.

Flow and transport parameters are those reported by Lu et al. (2011). All the aqueous species have the same effective diffusion, D_e, which is equal to 4.07·10^{-11} m^2/s. The bentonite porosity, ϕ, is equal to 0.407. The canister is assumed to have the same transport parameters, D_e and ϕ, as the bentonite.

The specific heat capacities of the bentonite and the canister are equal to 846 and 480 J/kg^{o}C, respectively. The saturated thermal conductivities of bentonite and steel canister are equal to 1.15, and 50 W/m^{o}C, respectively (ENRESA, 2000).

Table 2 lists the chemical composition of the initial bentonite porewater and the granitic boundary water of the bentonite-granite interface (Samper *et al.*, 2008a; Lu *et al.*, 2011). The initial porewaters are at chemical equilibrium with the minerals (Table 2). The initial chemical composition of the canister porewater is assumed to be the same as that of the bentonite porewater. The initial Al^{3+} concentrations in the bentonite and granite porewaters in the sensitivity runs which consider smectite dissolution are equal to 10^{-8} mol/L and $1.85 \cdot 10^{-8}$ mol/L, respectively (ENRESA, 2000).

The initial volume fractions of calcite (1%) and quartz (1%) in the bentonite are similar to those reported by Samper *et al.* (2008a). Gypsum, magnetite, siderite and goethite are not initially present in the system, but are allowed to precipitate. The cation exchange capacity (CEC) of the bentonite is 102 meq/100g (Fernández *et al.*, 2004). Cation selectivity coefficients for exchanged Ca^{2+}, Mg^{2+} and K^{+} in the reference run (Table 1) were derived from Samper *et al.* (2008a). These coefficients were calibrated to reproduce the concentrations of exchanged cations reported by Fernández *et al.* (2004) for the FEBEX bentonite. The selectivity coefficient for exchanged iron was taken from Tournassat (2003). Surface complexation reactions in the bentonite are modelled with the triple sorption site model of Bradbury and Baeyens (1997; 2005). The total concentration of sorption sites is 0.322 mol/L. The first type of sorption sites corresponds with the strong sites which have a large binding affinity but a small concentration (0.0079 mol/L). The

other two types are the weak #1 and #2 sites which have binding constants weaker than those of the strong sites although their concentrations (0.16 mol/L) are larger than those of the strong sites. Surface complexation and cation exchange reactions are not considered in the canister.

3.3 Computer code

Reactive transport calculations of the interactions of corrosion products with bentonite were performed with CORE^{2D} V4, a code for transient saturated and unsaturated water flow, heat transport and multicomponent reactive solute transport under both local chemical equilibrium and kinetic conditions in heterogeneous and anisotropic media (Samper *et al.,* 2009). The flow and transport equations are solved with Galerkin triangular finite elements and an Euler scheme for time discretization. The chemical formulation is based on the ion association theory and uses an extended version of Debye–Hückel equation (B-dot) for the activity coefficients of aqueous species. CORE^{2D} V4 relies on thermodynamic data from EQ3/6 (Wolery, 1992). It uses the sequential iteration approach to solve for chemical reactive solute transport. The iterative cycle is repeated until prescribed convergence criteria are attained (Xu *et al.,* 1999). The code has been widely used to model laboratory and in situ experiments (Samper *et al.,* 2008b; Zheng and Samper, 2008; Zheng *et al.,* 2010; 2011), model the interactions of corrosion products and bentonite (Samper *et al.,* 2008a; Lu *et al.,* 2011) and evaluate the long-term geochemical evolution of repositories in clay (Yang *et al.,* 2008, Samper *et al.,* 2014).

4. Model results for the reference scenario

The concentrations of the dissolved species in the bentonite porewater are significantly larger than those in the granite porewater, except for HCO_3^- (Table 2). Therefore, the dissolved concentrations of most of the species in the bentonite decrease with time and only that of HCO_3^- increases.

The canister is fully corroded at $t = 5 \cdot 10^4$ years. Model results show that canister corrosion leads to a marked increase in pH and the concentration of dissolved Fe^{2+} and a decrease in Eh, which reaches a minimum value of -6.7 V at r = 4.6 dm (1 cm from the canister) after 50000 y. Fig. 2 shows the time evolution of the concentration of dissolved Fe^{2+} and pH in the bentonite at radial distances, r = 4.6, 5.3 and 9.5 dm where r is measured from the axis of the disposal cell. The time evolution of the concentration of dissolved Fe^{2+} is directly linked to the concentrations of sorbed species. The dissolution/precipitation of Fe minerals and the competition of Fe^{2+} and H^+ for the sorption sites near the canister/bentonite interface lead to several pH and Eh fronts and fronts in the concentration of dissolved Fe^{2+}.

At r = 4.6 dm, the computed pH and the concentration of dissolved Fe^{2+} increase from their initial values until t = 45 years due to canister corrosion (Fig. 2). Siderite precipitates from t = 45 to t = 75 years, leading to a slight decrease of the concentration of dissolved Fe^{2+}. For $75 < t < 80$ years, magnetite precipitates sharply, siderite dissolves and the concentration of dissolved Fe^{2+} decreases abruptly when siderite is exhausted. At t = 80 years, magnetite dissolves quickly and consequently the pH increases more than a unit and the concentration of dissolved Fe^{2+} increases sharply. Later, the pH keeps increasing and reaches a peak value of 9.5 at $t = 2 \cdot 10^5$ years. The computed pH at $t = 10^6$ years gets below 9. The concentration of dissolved Fe^{2+} at $t = 10^5$ years becomes lower

than $5 \cdot 10^{-6}$ mol/L due to the aqueous diffusion of dissolved Fe^{2+} from the bentonite to the granite.

At r = 5.3 dm, the pH decreases sharply more than 2.5 units at t = 10^4 years while the concentration of dissolved Fe^{2+} decreases sharply due to the sorption of Fe^{2+} on weak #1 sites. Dissolved Fe^{2+} gets sorbed and releases protons (Fig. 2).

At r = 9.5 dm, the pH increases steadily and reaches a peak value similar to that computed at other locations.

The concentration of a conservative species such as Cl^- decreases with time because Cl^- diffuses from the bentonite into the granite (Figure 1S in Supplementary Material). The computed concentrations of dissolved cations show trends similar to those of Cl^-, but they are also subjected to mineral dissolution/precipitation and cation exchange processes.

Most of the released Fe^{2+} precipitates as magnetite and diffuses through the bentonite. Magnetite precipitation increases with time and progresses into the bentonite as Fe^{2+} diffuses from the canister into the bentonite (Fig. 3). The zone of bentonite affected by magnetite precipitation at t = 10^6 years has a thickness of 7 cm. The thickness of the siderite precipitation zone in the bentonite at t = 10^6 years is similar to that of magnetite precipitation (Fig. 3). However, siderite precipitation is much lower than magnetite precipitation due to the limited availability of dissolved bicarbonate. The concentration of precipitated magnetite ranges from 5 to 70 mol/L while that of siderite is about 1 mol/L at t = 10^5 years. Goethite does not precipitate.

Calcite dissolves in most of the bentonite except near the interface canister-bentonite where it precipitates due to the increase in pH induced by canister corrosion. Far from this interface, the concentration of dissolved Ca^{2+} decreases due to solute diffusion from the bentonite into the granite. Such a decrease leads to a slight calcite dissolution. The dissolution/precipitation of quartz and gypsum is very small.

Only a small part of the Fe^{2+} released by canister corrosion is sorbed at exchanged sites. The time evolution of the concentration of exchanged Fe^{2+} is similar to that of sorbed and dissolved Fe^{2+}. The concentration of exchanged Ca^{2+} increases at t = 1 Ma while those of Na^{+} and Mg^{2+} decrease.

The model assumes that the porosity is constant in time. However, it may change due to the effect of mineral dissolution/precipitation. Such changes in porosity were calculated from the computed concentrations of dissolved/precipitated minerals. The porosity at the canister-bentonite interface is half of its initial value at $t = 10^4$ years for a corrosion rate of 2 μm/y (Fig. 4). The precipitation of the corrosion products near the canister leads to a significant decrease of bentonite porosity. At the end of the simulation, the porosity reduces to zero in a band of 2.5 cm thickness near the canister-bentonite interface. The changes in porosity are negligible for r > 5.25 dm. The thickness of bentonite affected by a porosity reduction larger than 10% increases with time and is equal to 7 cm at t = 1Ma (Fig. 5). The changes in porosity in the rest of the buffer are negligible.

5. Sensitivity to model parameters

5.1 Corrosion rate

Sensitivity runs were performed for corrosion rates ranging from 0.1 to 5 μm/year. The larger the corrosion rate, the faster the increase in the concentration of dissolved Fe^{2+} and the pH (Fig. 6) and the sooner and the closer to the canister-bentonite interface the Fe^{2+} concentration, pH, Eh and sorption and mineral dissolution/precipitation fronts take place. The larger the corrosion rate, the larger the magnetite and siderite concentration near the canister-bentonite interface but the smaller their penetration into the bentonite. Therefore, the larger the corrosion rate, the smaller the thickness of affected bentonite (Fig. 7). The thickness ranges from less than 5 cm for a corrosion rate of 5 μm/year to nearly 12 cm for a rate of 0.5 μm/year. The results for the smallest corrosion rate of 0.1 μm/year show clear differences from those of the other corrosion rates. The smallest corrosion rate leads to the largest pH (above 10), the largest thickness of bentonite affected by porosity reduction and a single and smooth sorption front.

5.2 Effective diffusion coefficient

Two sensitivity runs were performed to evaluate the sensitivity of the predictions to changes in the effective diffusion, D_e, of the bentonite. Except for the dissolved Fe^{2+}, the computed concentrations of most dissolved species lack sensitivity to changes in D_e by a factor of 0.5 and 2, respectively. The larger the D_e, the smoother the increase of the concentration of dissolved Fe^{2+} and the larger the thickness of altered bentonite which varies from 4 to 10 cm in the considered range of the D_e (Fig. 7).

5.3 Water flow in the granite

The groundwater flow through the granite, Q, could be larger than the value adopted for the reference run (0.01 L/year) in areas where the rock is more fractured. Sensitivity runs were performed for values of Q ranging from 0.01 to 0.1 L/y. The solute flux from the bentonite into the granite is controlled mostly by the advective transport through the granite. Therefore, the computed concentrations of most of the dissolved species are sensitive to changes in Q. The larger the Q, the faster the decrease of the dissolved concentrations (Figure 1S in Supplementary Material). The computed pH at t = 400 years is slightly sensitive to changes in Q. When Q increases, more dissolved Fe^{2+} gets out of the system and more dissolved HCO_3^- becomes available. The decrease of the concentration of dissolved Fe^{2+} decreases magnetite precipitation while the increase of the concentration of dissolved HCO_3^- increases siderite precipitation. The sorption and mineral dissolution/precipitation fronts become smoother when Q increases. The larger the Q, the smaller the thickness of bentonite with precipitation of corrosion products. The bentonite thickness affected by the porosity reduction decreases when Q increases (Fig. 7). Such thickness decreases from 7 to 3 cm when Q increases by a factor of 10.

5.4 Cation exchange selectivities

A sensitivity run was performed to evaluate the sensitivity of the predictions to changes in cation selectivities (Table 1). The changes in the selectivities only affect the concentrations of exchanged cations, especially those of Mg^{2+} and Ca^{2+}. The concentration of exchanged iron is so small that the changes in selectivities have a negligible effect on the concentrations of dissolved and exchanged Fe^{2+}.

5.5 Bentonite and granite porewater

Given the difficulties of deriving reliable data on saturated bentonite porewater, a sensitivity run was performed by considering the chemical compositions of the initial bentonite porewater and the granitic boundary water proposed by Samper et al. (2008b) (Table 2). The main corrosion product in the sensitivity run is also magnetite. The concentration of magnetite near the canister-bentonite interface computed in the sensitivity run is larger than that of the reference run while the thickness of the zone where magnetite penetrates is half of that computed in the reference run. The thickness of the bentonite zone affected by pore clogging in the sensitivity run with the modified chemical composition is also lower than that of the reference run (Fig. 7).

6. Sensitivity runs for conceptual model uncertainties

Sensitivity runs were performed to analyse the uncertainties due to the simplifications of the conceptual model. The sensitivity runs addressed the following features: 1) The thermal field across the bentonite barrier; 2) The dependence of the corrosion rate on temperature; 3) The dependence of the corrosion rate on the chemical conditions; 4) The kinetic magnetite precipitation and 5) The kinetic dissolution of smectite and the neoformation of Fe-clay minerals and zeolites.

6.1 Thermal transient

The thermal gradient across the engineered barrier system (EBS) may last for thousands of years and therefore may influence the geochemical evolution of the bentonite. A sensitivity run was performed by accounting for the thermal field across the bentonite barrier. The heat transport through the bentonite buffer was solved and the computed

temperatures were used to update the temperature-dependent chemical parameters such as the equilibrium constants and the activity coefficients.

The time evolution of temperature was prescribed at the canister/bentonite interface according to the thermal simulations of ENRESA (2000). The temperature at the canister is 97 ºC at t = 24 years and then decreases smoothly (Fig. 8). The temperature at the canister/bentonite interface is equal to 30ºC at t = 1 Ma. The granitic boundary porewater is considered at a constant temperature of 30 ºC.

The computed concentration of dissolved Fe^{2+} and the pH for the non-isothermal run are smaller than those of the isothermal simulation for $t < 10^5$ years (Fig. 9). The fronts of pH and Eh, concentration of dissolved Fe^{2+}, sorption and mineral dissolution/precipitation are similar to those of the isothermal run, but they take place before. Magnetite precipitation at 1 Ma is almost the same as in the isothermal reference run.

6.2 Temperature-dependent corrosion rate

The dependence of the corrosion rate on temperature was analysed by performing a sensitivity run which accounts for the thermal transient and also for the temperature dependence of the corrosion rate. Carbon-steel canister dissolves according to the kinetic law of Eq. (3) with an activation energy equal to 11 KJ/mol (Feron *et al.*, 2008).

The results of the sensitivity run which accounts for the thermal field and the influence of temperature on corrosion show that the corrosion rate increases from 2 to 4.75 μm/y

and then decreases smoothly (Fig. 8). The corrosion rate at t = $1.3 \cdot 10^4$ years is lower than 2.5 μm/y. Therefore, canister corrosion in this run is faster than in the reference run.

The computed concentration of dissolved Fe^{2+} and the pH in this sensitivity run increase initially faster than those of the reference run. The computed curves of pH coincide at t = 10^3 years (Fig. 9). The chemical fronts are similar to those computed for the reference run and the sensitivity run accounting for the thermal transient and a constant kinetic rate. However, they take place sooner than those of the run with a constant corrosion rate.

The precipitation of corrosion products occurs before, and their penetration in the sensitivity run is lower than in the reference run. The precipitation of magnetite at 1 Ma is slightly lower than that of the isothermal reference run and the non-isothermal run which accounts for a constant corrosion rate. The thickness of the zone where magnetite precipitates in the bentonite is 6 cm.

The porosity of the bentonite near the canister decreases faster than those computed with the isothermal and non-isothermal runs with constant corrosion rates. The thickness of the bentonite band affected by a decrease of porosity is equal to 7 cm at t = 10^4 years and 6 cm at t = 1 Ma.

6.3 Dependence of the corrosion rate on the chemical conditions

There is no well-established geochemical model which considers the effect of the ambient chemical conditions (pH, Eh, Fe, …) on the corrosion rate in reactive transport models. The dependence of the corrosion rate on pH, Eh and the concentration of Fe^{2+} was

analysed by performing an isothermal sensitivity run similar to the reference run, but accounting for a variable corrosion rate, $r_{m,}$ which depends on the saturation index Ω_m in Eq. (3). The corrosion rate was computed with Eq. (3) with $\eta = 1$ and $\theta = 1$. Even though the corrosion reaction is not likely to reach chemical equilibrium at the expected conditions of the repository, the use of Eq. (3) for canister corrosion provides a way to account for the effect of the ambient chemical conditions on the corrosion rate.

Model results show that canister corrosion slows down at $t = 10^3$ years and the canister is fully corroded at $t = 8 \cdot 10^5$ years. This reduction of the corrosion rate leads to important changes in the patterns of the concentration of dissolved Fe^{2+}, pH, Eh, sorption and mineral dissolution/precipitation at $t = 10^3$ years. The maximum pH is larger than 10. Magnetite and siderite precipitation in the sensitivity run is significantly smaller than that of the reference run. The thickness of the zone where these minerals precipitate is significantly larger than that of the reference run, although the cumulative amount of mineral precipitation near the canister is smaller (Fig. 10). The reduction of the porosity due to mineral dissolution/precipitation affects a thickness of bentonite of about 45 cm. However, the thickness of the bentonite band with a 50% reduction in porosity is equal to 14 cm. This behaviour is similar to that observed in the sensitivity run with the smallest constant corrosion rate (0.1 μ/m).

6.4 Kinetically-controlled magnetite precipitation

The reference run assumes magnetite precipitation at chemical equilibrium. However, both the experimental data and the model results of laboratory corrosion tests performed

by Ciemat show that the migration of corrosion products should be modelled with kinetic magnetite precipitation (Samper *et al.*, 2014). A sensitivity run was performed which accounts for kinetic magnetite precipitation. The precipitation rate, r_m, was calculated with Eq. (3) with $k_m = 9.53 \cdot 10^{-11}$ mol/m^2/s, $\eta = 1$ and $\theta = 0.1$ (De Windt and Torres, 2009).

Model results are sensitive to changes in the magnetite reactive surface area. The sequential iterative approach showed a slow convergence for large reactive surfaces. Figure 2S (Supplementary Material) shows the computed cumulative precipitation of magnetite at 10^5 years for the reference run, and two sensitivity runs accounting for kinetic magnetite precipitation using two reactive surface areas. The zone of magnetite precipitation decreases and, therefore, the thickness of the altered bentonite decreases significantly when magnetite kinetics is considered. The larger the reactive surface area, the thinner the zone of bentonite affected by canister corrosion.

6.5 Smectite dissolution and neoformation of analcime and cronstedtite

Smectite dissolution is commonly disregarded in short to medium-term geochemical models (e.g. lab and in-situ tests) because it is not considered relevant in the short term. However, smectite dissolution could be relevant for the long-term geochemical evolution of the engineered barrier system.

A sensitivity run was performed by accounting for the kinetic dissolution of smectite and the kinetic precipitation of analcime. Smectite dissolution and analcime precipitation take

place in the entire bentonite barrier in very small concentrations. Only 0.2% (vol) of the smectite dissolves at t = 1 Ma. Therefore, the total amount of dissolved smectite is not significant. The concentrations of the dissolved species are not sensitive to smectite dissolution and analcime precipitation. On the other hand, the precipitation of corrosion products is sensitive to smectite dissolution and analcime precipitation. The thickness of the altered bentonite decreases 3 cm when these two minerals are considered.

A sensitivity run was performed by considering the precipitation of cronstedtite at chemical equilibrium besides the dissolution of smectite and the precipitation of analcime. Cronstedtite precipitates near the canister/bentonite interface reducing slightly the precipitation of analcime (Figure 3S in Supplementary Material). The thickness of the bentonite zone where cronstedtite precipitates is equal to 9 cm. Smectite dissolution/precipitation is not significantly influenced by the precipitation of cronstedtite. The thickness of bentonite affected by the porosity reduction is similar to that of the reference run.

The errors in total mass balance are equal to 0.26 % for Si and $7 \cdot 10^{-4}$ % for Al. The errors in the dissolved mass balance could be larger because most of the Si and Al are present in mineral phases.

6.6 Canister Porosity

A sensitivity run was performed by changing the porosity of the canister from 0.407 to 0.2. This change leads to slight changes in the computed pH, Eh and the concentration of dissolved Fe^{2+}. The propagation of the sorption and mineral dissolution/precipitation

fronts is slightly delayed compared to the base run. Magnetite precipitation in the sensitivity run is slightly larger than in the base run. The thickness of bentonite affected by the precipitation of corrosion products increases 2 cm compared to the base run.

7. Comparison with the results of other models

Most THC modelling studies of the interactions of corrosion products and compacted bentonite lead to the following results (Savage, 2012): 1) Magnetite is the main steel corrosion product, and 2) The clay minerals of the bentonite are altered to a mixture of non-swelling Fe-phyllosilicates and zeolites.

Our results share many of the features of the results of Bildstein *et al.* (2006). Magnetite is the main corrosion product while siderite precipitation is much lower than magnetite precipitation. The reduction of bentonite porosity due to mineral precipitation near the canister/bentonite interface could result in the clogging of the bentonite pores. The bentonite thickness affected by porosity reduction increases with time and is equal to 7 cm at t = 1Ma. Cronstedtite precipitates near the canister/bentonite interface. Similar to Wersin *et al.* (2007), our calculations show that the extent of the bentonite zone affected by mineral transformations is limited to a few cm for very long times. Marty *et al.* (2010a) recognized that their calculations of the long-term alteration of the engineered bentonite barrier might overestimate the transformation rate of the minerals because they assumed a constant temperature of 100 °C throughout the simulation time. Our model is more realistic because it takes into account the time evolution of the temperature. The numerical results presented here cannot be compared directly to those of Savage *et al.*

(2010a) because our model consider neither the Ostwald step nor the time variation of the reactive surface areas of the secondary minerals. Ngo et al. (2014) found that the changes in porosity and mineral transformations in the iron-bentonite system are larger when mineral particles of different sizes are considered for calculating the surface areas of the primary minerals. The alteration of the iron-bentonite system concerns two zones in direct contact with the geological groundwater and steel overpack, but for the iron-COx claystone the mineralogical modifications are predicted to occur in the entire bentonite barrier. Our model results agree with those of Ngo et al. (2014) in the predicted reduction of bentonite porosity and the main mineral modifications.

8. Conclusions

A nonisothermal reactive transport model for the long-term (1 Ma) interactions of the corrosion products and compacted bentonite in a HLW repository in granite has been presented. Canister corrosion causes an increase in the pH and the concentration of dissolved Fe^{2+} of the bentonite porewater. Iron precipitates as magnetite and siderite and sorbs via cation exchange and surface complexation on weak sites. The largest pH in the bentonite is almost 9.5 at $2 \cdot 10^5$ years. Several fronts are observed in the concentration of dissolved Fe^{2+}, pH and Eh which are related to sorption and mineral dissolution/precipitation fronts. Magnetite is the main corrosion product and its precipitation reduces significantly the porosity of the bentonite barrier near the canister and could even clog the pores. The thickness of the bentonite zone affected by the decrease of porosity increases with time and is equal to 7 cm at t = 1 Ma.

A detailed sensitivity analysis has been performed to changes in model parameters and conceptual model assumptions. The larger the corrosion rate, the larger the magnetite and siderite concentration near the canister-bentonite interface but the smaller their penetration into the bentonite. Therefore, the larger the corrosion rate, the faster the porosity reduction near the canister but the smaller the thickness of affected bentonite. This thickness ranges from < 5 cm for a corrosion rate of 5 μm/year to nearly 12 cm for 0.5 μm/year. The larger the effective diffusion, D_e, the larger the thickness of the bentonite where magnetite, siderite and calcite precipitate and the thicker the bentonite affected by pore clogging. This thickness varies from 4 to 10 cm in the considered range of the D_e. The bentonite thickness affected by the porosity reduction decreases when the ground water flow through the granite, Q, increases. Such thickness decreases from 7 cm to 3 cm when Q increases by a factor of 10. The changes in the bentonite cation exchange selectivities do not affect the computed pH, Eh and the concentrations of other dissolved and precipitated species. The computed magnetite concentration near the canister-bentonite interface is sensitive to changes in the initial chemical composition of the bentonite porewater. By accounting for the dependence of the corrosion rate on the chemical conditions, the thickness of altered bentonite is significantly larger than that of the reference run although the cumulative amount of mineral precipitation near the canister is smaller. The thermal transient and the effect of temperature on the corrosion rate do not have a very significant influence on the geochemical evolution of the bentonite barrier. The thickness of altered bentonite decreases when kinetic magnetite precipitation is considered. Such thickness decreases 3 cm when smectite dissolution and analcime

precipitation are taken into account. However, it is similar to that of the reference run when cronstedtite is considered besides smectite dissolution and analcime precipitation.

The conclusions of our simulations are consistent for the most part with those reported by other numerical analyses of the interactions of corrosion products and compacted bentonite in engineered barrier systems at similar chemical conditions. However, there are differences in the geochemical systems and the hypotheses used by Savage *et al.* (2010a).

The results of the long-term geochemical evolution of the corrosion products and compacted bentonite presented here could be improved by: 1) Considering the adsorbed, the interlayer and the free water; 2) Allowing for different effective diffusion coefficients for each chemical species; 3) Allowing for the dynamic update of the reactive surface areas of the minerals and the bentonite porosity to account for pore clogging; 4) Simulating the progressive corrosion of the canister surface by assuming that the corrosion front penetrates into the canister as the corrosion progresses until all the canister has been corroded as reported by Lu (2009); 5) Taking into account kinetic magnetite precipitation; and 6) Accounting for the precipitation of other Fe-phylosilicates such as chlorite and berthierine, Fe-rich smectites such as saponite and zeolites such as phillipsite, chabazite and merlionite.

Acknowledgements

The research leading to this work has received funding from the PEBS Project of the European Atomic Energy Community's Seventh Framework Programme (FP7/2007-

2011) under grant agreement 232598. This work was partly funded by ENRESA (Spain), the Spanish Ministry of Economy and Competitiveness (Project CGL2012-36560), FEDER funds and the Galician Regional Government (Project 10MDS118028PR and Fund 2012/181 from "Consolidación e estruturación de unidades de investigación competitivas", Grupos de referencia competitiva). We thank the comments, corrections and suggestions of the two anonymous reviewers which contributed to the improvement of the paper.

References

Bildstein, O., Trotignon, L., Perronnet, M., Jullien, M., 2006. Modelling iron-clay interactions in deep geological disposal. Physics and Chemistry of the Earth 31, 618–625.

Bradbury, M.H., Baeyens, B., 1997. A mechanistic description of Ni and Zn sorption on Na-montmorillonite. Part II: Modelling. Journal of Contaminant Hydrology 27, 223-248.

Bradbury, M.H., Baeyens, B., 2005. Modelling the sorption of Mn(II), Co(II), Ni(II), Zn(II), Cd(II), Eu(III), Am(III), Sn(IV), Th(IV), Np(V) and U(VI) on montmorillonite: Linear free energy relationships and estimates of surface binding constants for some selected heavy metals and actinides. Geochimica et Cosmochimica Acta 69, 875-892.

De Windt, L., Torres, E., 2009. Modélisation d'expériences en cellule reproduisant les conditions THC d'une alvéole de déchets HAVL. Rapport Technique R201009LDEWI. Accord spécifique IRSN/ARMINES.

ENRESA, 2000. Evaluación del comportamiento y de la seguridad de un almacenamiento de combustible gastado en una formación granítica. ENRESA Tech Report 49-1PP-M-15-01. (In Spanish).

Fernández, A., Baeyens, B., Bradbury, M., Rivas, P., 2004. Analyses of the porewater chemical composition of a Spanish compacted bentonite used in a engineered barrier. Physics and Chemistry of the Earth 29, 105-118.

Fernández, A., Cuevas, J., Mäder, U.K., 2009. Modelling concrete interaction with a bentonite barrier. . European Journal of Mineralogy 21, 177-191.

Féron, D., Crusset, D., Gras, J.-M., 2008. Corrosion issues in nuclear waste disposal. Journal of Nuclear Materials, 379, 16–23.

Lu, C., 2009. Reactive Transport Models in Nuclear Waste Disposal and Acid Mine Drainage. Ph.D. Thesis. University of A Coruña, Spain.

Lu, C., Samper, J., Fritz, B., Clement, A., Montenegro, L., 2011. Interactions of corrosion products and bentonite: An extended multicomponent reactive transport model, Physics and Chemistry of the Earth 36, 1661–1668, doi: 10.1016/j.pce.2011.07.013.

Marty, N.C.M, Fritz, B., Clément, A., Michau, N., 2010a. Modelling the long term alteration of the engineered bentonite barrier in an underground radioactive waste repository. Applied Clay Science, 47, 82-90.

Marty, N., Claret, F., Gaboreau, S., Cochepin, B., Munier, I., Michau, N., Gaucher, E. C., Burnol, A., 2010b. Dual alteration of bentonite by iron corrosion and concrete interaction under high temperature conditions. In Clays in Natural and Engineered Barriers for Radioactive Waste Confinement, Nantes, France, pp. 473–474.

Montes-H, G., Fritz, B., Clement, A., Michau, N., 2005. Modeling of transport and reaction in an engineered barrier for radioactive waste confinement. Applied Clay Science 29, 155-171.

Ngo, V.V., Delalande, M., Clément, A., Michau, N., Fritz, B., 2014. Coupled transport-reaction modeling of the long-term interaction between iron, bentonite and

Callovo-Oxfordian claystone in radioactive waste confinement systems. Applied Clay Science 101, 430–443.

Ortiz, L., Volckaert, G., Mallants, D., 2002. Gas generation and migration in Boom Clay, a potential host rock formation for nuclear waste storage. Eng. Geol. 64, 287–296.

Rozalén, M.L., Huertas, F.J., Brady, P.V., Cama, J., García-Palma, S., Linares, J., 2008. Experimental study of the effect of pH on the kinetics of montmorillonite dissolution at 25 ºC. Geochimica et Cosmochimica Acta 72, 4224-4253.

Samper, J., Lu, C., Montenegro, L., 2008a. Coupled hydrogeochemical calculations of the interactions of corrosion products and bentonite. Physics and Chemistry of the Earth 33, S306–S316, doi:10.1016/j.pce.2008.10.009.

Samper, J., Zheng, L., Fernández, A.M., Montenegro, L., 2008b. Inverse modeling of multicomponent reactive transport through single and dual porosity media. Journal of Contaminant Hydrology 98, 115–127.

Samper, J., Xu, T., Yang, C., 2009. A sequential partly iterative approach for multicomponent reactive transport with CORE2D. Computational Geosciences. doi: 10.1007/s10596-008-9119-5.

Samper J, A Mon, L Montenegro & A Naves. 2014. Long-term THCM simulations of the interactions of compacted bentonite in contact with concrete and carbon steel

in a HLW repository in clay; International Conference on the Performance of Engineered Barriers: Backfill, Plugs & Seals, Physical and Chemical Properties, Behaviour & Evolution, A Schäfers & S Fahland Ed. BGR, Hannover, Germany, pp. 347-357.

Savage, D., Watson, C., Benbow, S., Wilson, J., 2010a. Modelling iron/bentonite interactions. Applied Clay Science 47, 91-98.

Savage, D., Arthur, R., Watson, C, Wilson, J., 2010b. An Evaluation of Models of Bentonite Pore Water Evolution. Swedish Radiation Safety Authority. Report number: 2010:12

Savage, D., 2012. Prospects for coupled modelling. STUK-TR 13. Radiation and Nuclear Safety Authority.

Tournassat, C., 2003. Cations–clay interactions: The Fe(II) case. Application to the problematic of the French deep nuclear repository field concept. Ph.D. Dissert. Grenoble, France.

Wersin, P., Birgersson, M., Olsson, S., Karnland, O., Snellman, M., 2007. Impact of corrosion-derived iron on the bentonite buffer within the KBS-3H disposal concept – the Olkiluoto site as case study. Posiva Report 2007-11.

Wilkin, R.T., Barnes, H.L., 1998. Solubility and stability of zeolites in aqueous solution: I. Analcime, Na-, and K-clinoptilolite. American Mineralogist 83, 746-761.

Wolery, T.J., 1992. EQ3/6, a software package for geochemical modeling of aqueous systems: Package overview and installation guide (version 7.0). Technical Report UCRL-MA-110662-Pt 1. Lawrence Livermore National Laboratory, CA, USA.

Xu, T., Samper, J., Ayora, C., Manzano, M., Custodio, E., 1999. Modeling of nonisothermal multicomponent reactive transport in field scale porous media flow systems. Journal of Hydrology 214, 144–164.

Xu, T., R. Senger, and S. Finsterle, 2008, Corrosion-induced gas generation in a nuclear waste repository: Reactive geochemistry and multiphase flow effects, Applied Geochemistry, v.23, p. 3423-3433.

Yang, C., Samper, J., Montenegro, L., 2008. A coupled non-isothermal reactive transport model for long-term geochemical evolution of a HLW repository in clay. Environmental Geology 53, 1627–1638, doi: 10.1007/s00254-007-0770-2.

Zheng, L., Samper, J., 2008. Coupled THMC model of FEBEX mock-up test. Physics and Chemistry of the Earth 33, S486–S498, doi:10.1016/j.pce.2008.10.023.

Zheng, L, Samper, J., Montenegro, L., Fernández, AM., 2010. A coupled THMC model of a heating and hydration laboratory experiment in unsaturated compacted FEBEX bentonite. Journal of Hydrology 386, 80-94, doi: 10.1016/j.jhydrol.2010.03.009.

Zheng, L, Samper, J., Montenegro, L., (2011). A coupled THC model of the FEBEX in situ test with bentonite swelling and chemical and thermal osmosis. Journal of Contaminant Hydrology 126, 45-60.

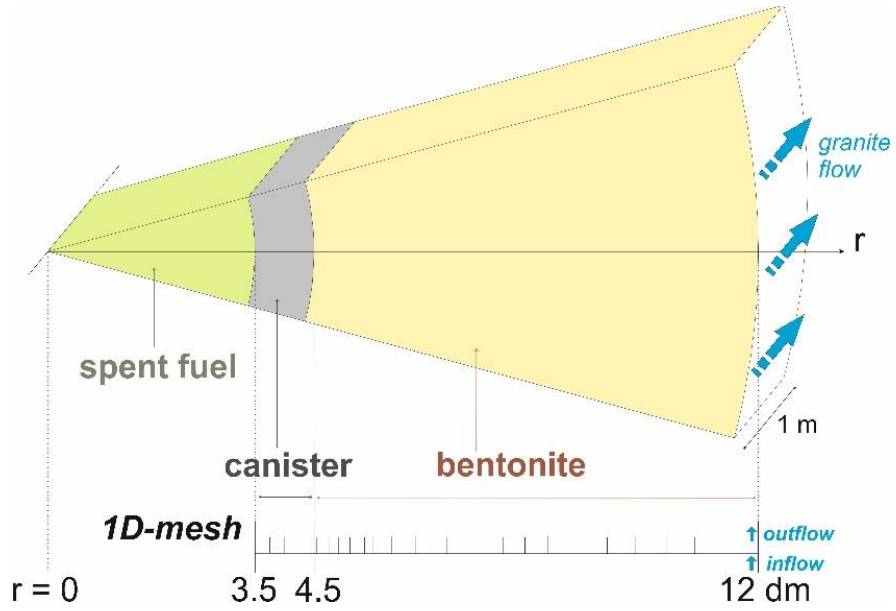

Fig. 1. Sketch of the engineered barrier system and 1D finite element grid of the axisymmetric model.

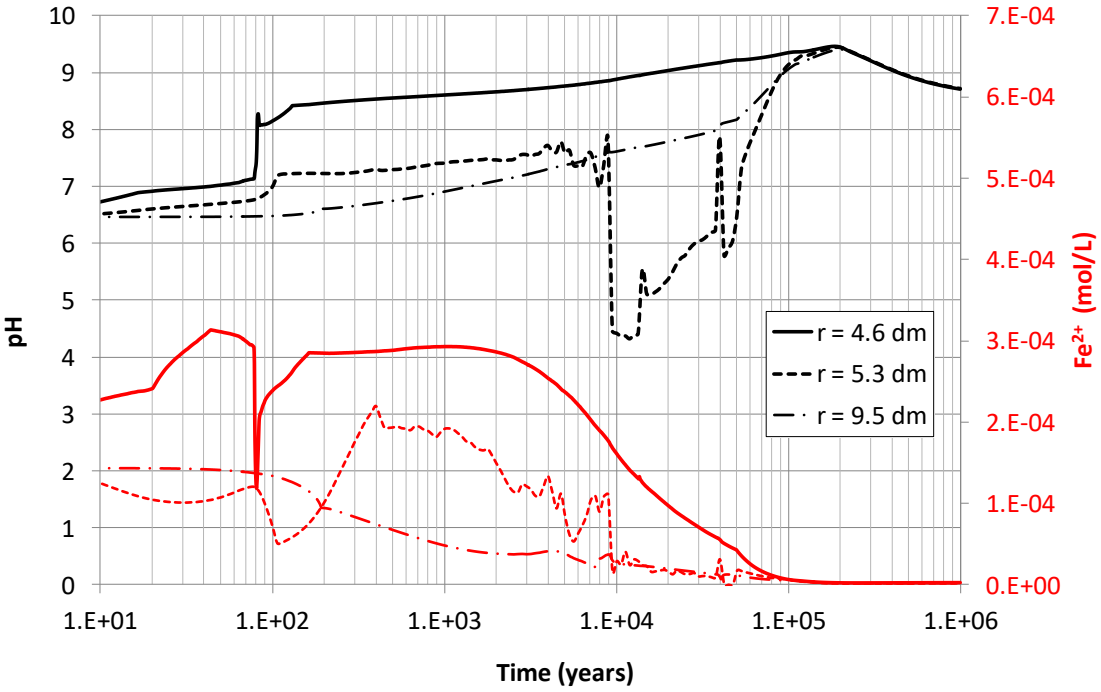

Fig. 2 Time evolution of the computed pH and the concentration of dissolved Fe^{2+} in the bentonite at radial distances, r, equal to 4.6, 5.3 and 9.5 dm.

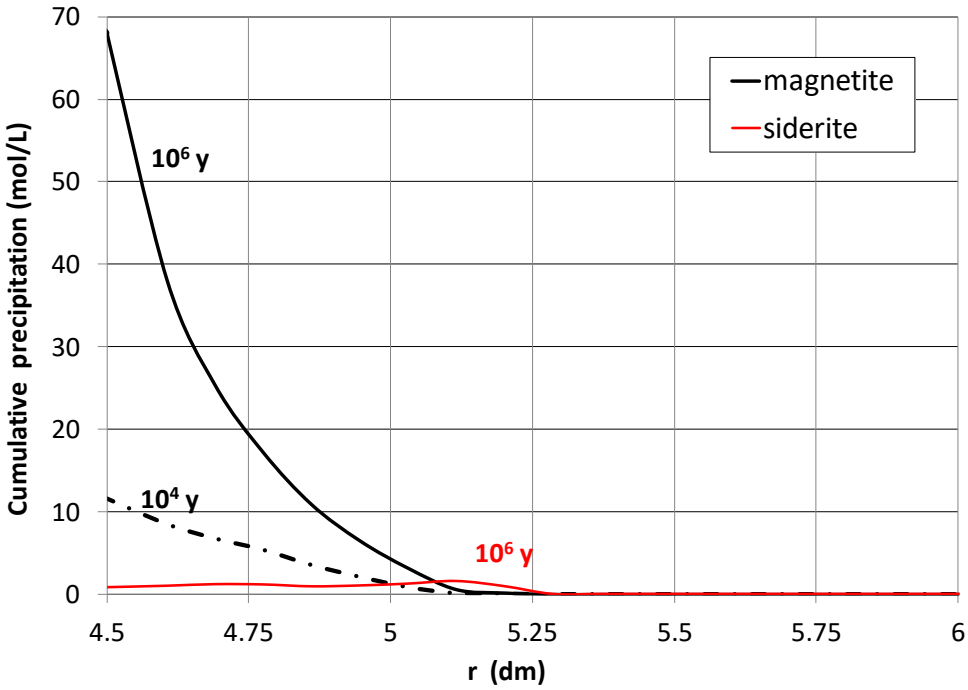

Fig. 3. Radial distribution of the concentration of cumulative precipitated magnetite at t = 10^4 and 10^6 years and siderite at t = 10^6 years. r is the radial distance from the axis of the disposal cell.

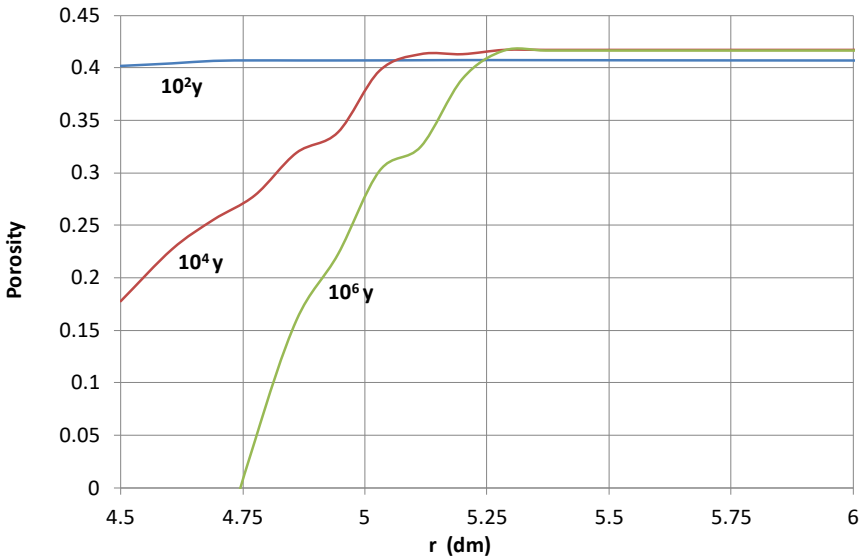

Fig. 4. Radial distribution of the computed bentonite porosity which changes due to mineral dissolution/precipitation at selected times.

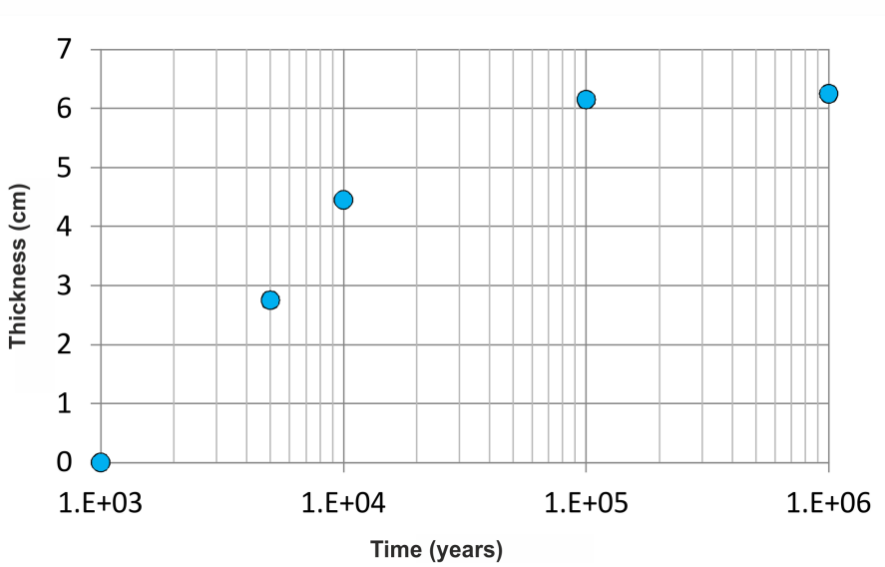

Fig. 5. Time evolution of the thickness of the bentonite affected by a porosity reduction larger than 10%.

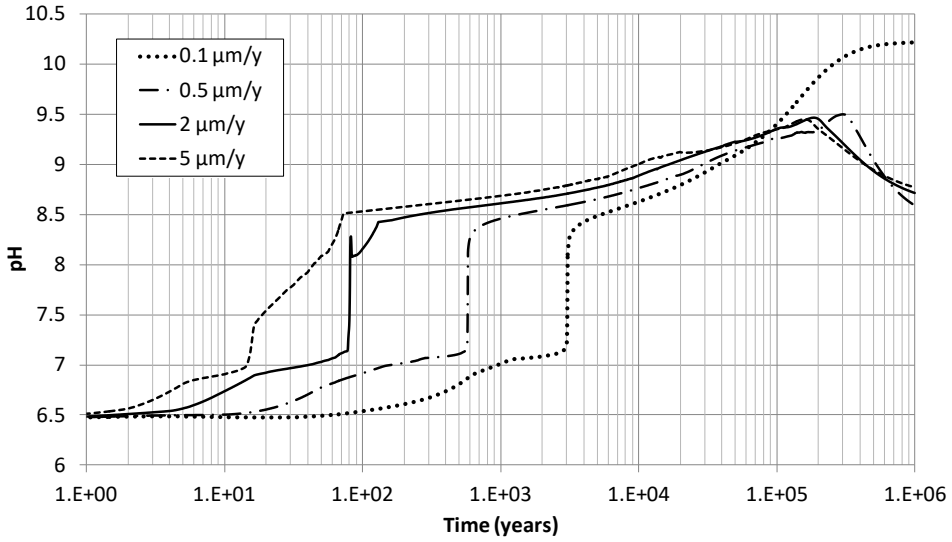

Fig. 6. Sensitivity of the time evolution of the computed pH at r = 4.6 dm to changes in the corrosion rate.

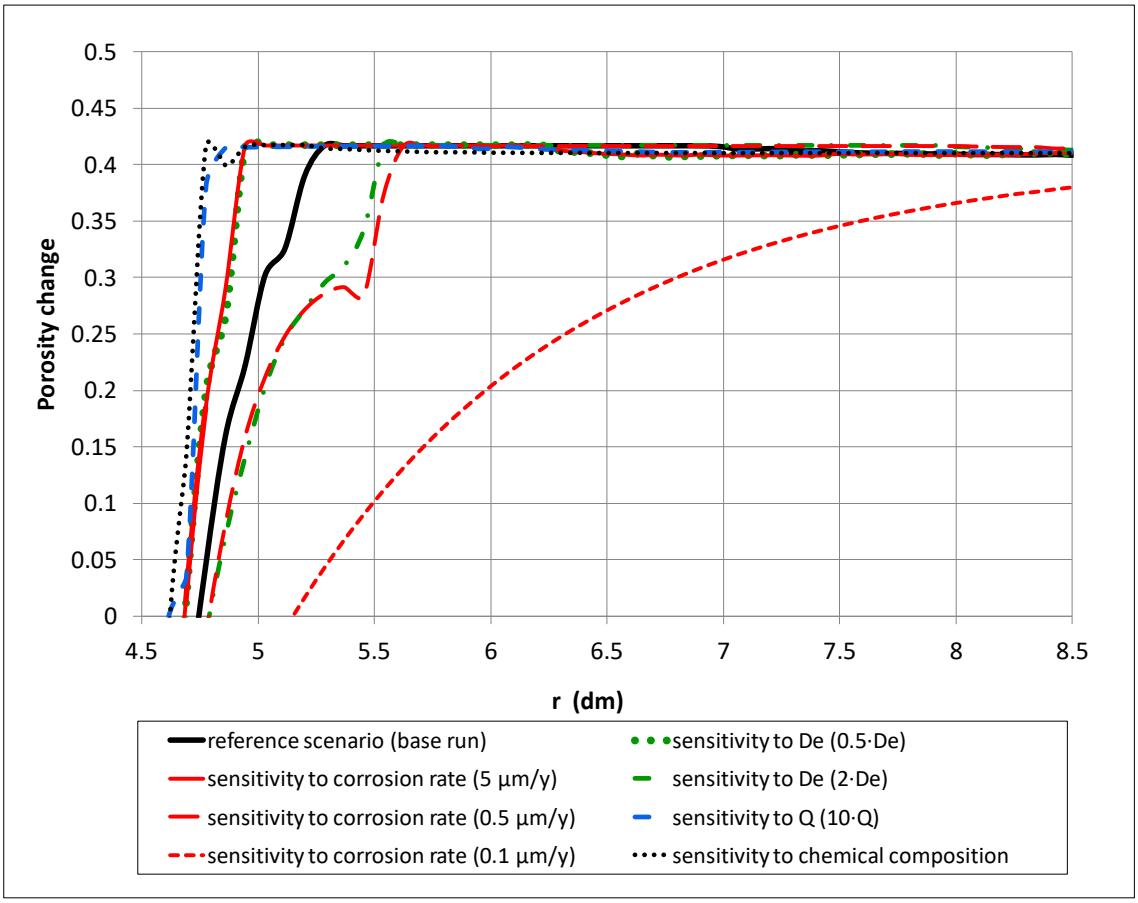

Fig. 7. Sensitivity of the radial distribution of the computed bentonite porosity at t = 1 Ma to changes in the corrosion rate, the effective diffusion through the bentonite, D_e, the groundwater flow, Q, and the initial chemical compositions of the bentonite and granite porewaters.

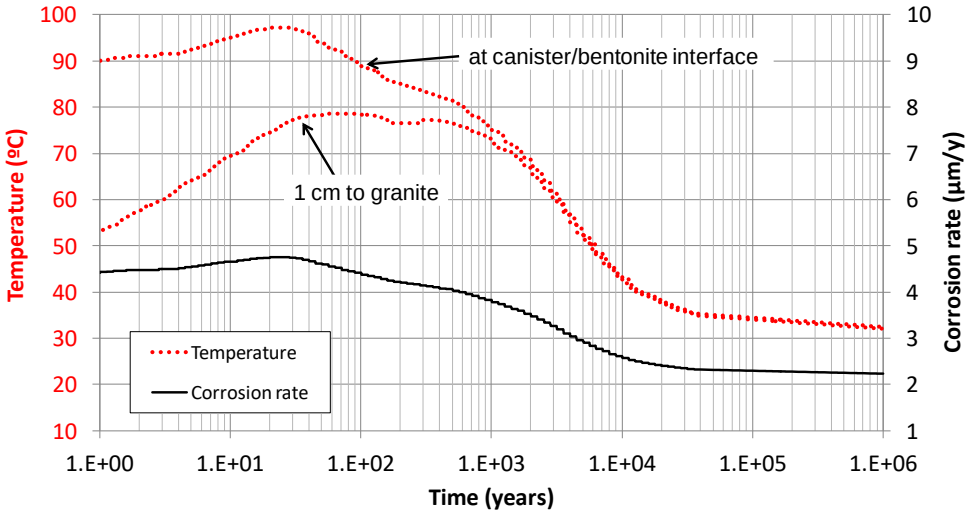

Fig. 8. Time evolution of the computed temperatures at the canister/bentonite interface and in a point of the bentonite located 1 cm from the granite and corrosion rate for the sensitivity run which accounts for the thermal transient and the dependence of the corrosion rate on temperature.

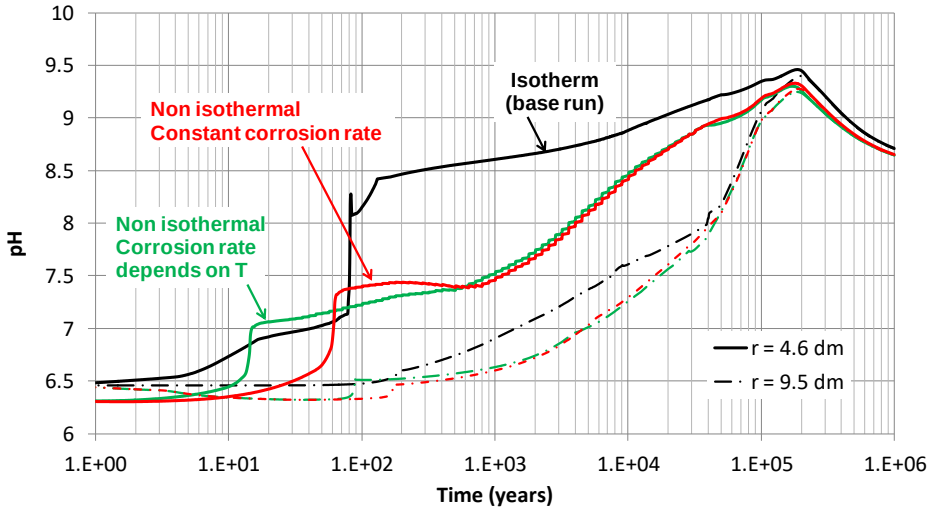

Fig. 9. Time evolution of the computed pH in the bentonite at r = 4.6 and 9.5 dm for the reference isothermal run and the sensitivity runs which account for the thermal transient and the constant temperature-dependent corrosion rates.

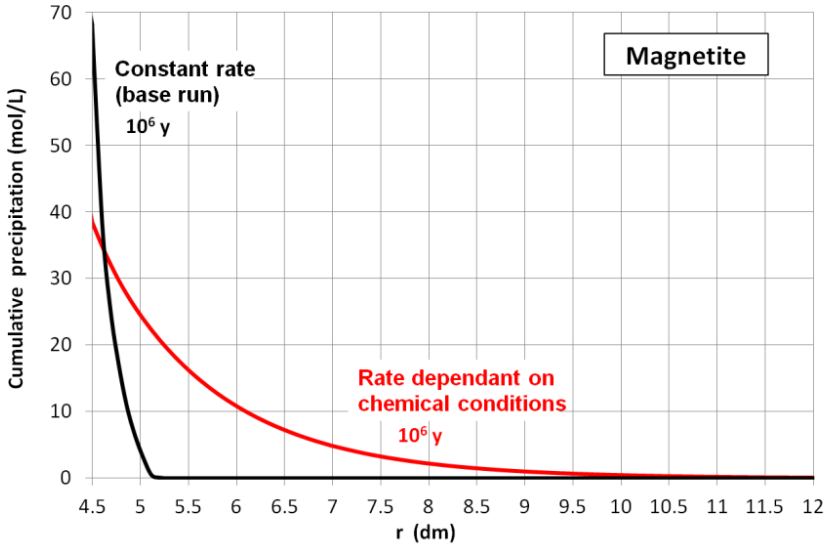

Fig. 10. Radial distribution of the concentration of cumulative precipitated magnetite at t = 1 Ma computed with the reference run and the sensitivity run with a corrosion rate dependent on the chemical conditions.

Table 1. Equilibrium constants for minerals (Wolery, 1992; Fernández *et al.*, 2009; Savage *et al.*, 2010a; Wilkin and Barnes, 1998), protolysis constants for surface complexation reactions for a triple-site model (Bradbury and Baeyens, 2005), and selectivity constants for cation exchange reactions for the reference run (Samper *et al.*, 2008a; Tournassat, 2003) and the calibrated values at 25ºC.

Minerals	**Log K (25°C)**
$Carbon\ steel + 2H^+ + 0.5O_2(aq) \rightleftarrows Fe^{2+} + H_2O$	59.033
$Calcite + H^+ \rightleftarrows Ca^{2+} + HCO_3^-$	1.8487
$Gypsum \rightleftarrows Ca^{2+} + SO_4^{2-} + 2H_2O$	-4.4823
$Quartz \rightleftarrows SiO_2(aq)$	-3.9993
$Magnetite + 6H^+ \rightleftarrows 3Fe^{2+} + 0.5O_2(aq) + 3H_2O$	-6.5076
$Siderite + H^+ \rightleftarrows Fe^{2+} + HCO_3^-$	-0.1920
$Goethite + 2H^+ \rightleftarrows Fe^{2+} + 1.5H_2O + 0.25O_2(aq)$	-7.9555
$Smectite + 6.56H^+ \rightleftarrows 0.135Na^+ + 0.055K^+ + 0.125Ca^{2+} + +0.525Mg^{2+} + 1.69Al^{3+} + 3.86SiO_2(aq) + 4.82H_2O$	6.26
$Analcime + 4H^+ \rightleftarrows Na^+ + Al^{3+} + 2SiO_2(aq) + 3H_2O$	6.7833
$Cronstedtite + 10H^+ \rightleftarrows 2Fe^{2+} + 2Fe^{3+} + SiO_2(aq) + 7H_2O$	16.2603
Cation exchange	**$K_{Na\text{-}cation}$ Reference /Calibrated**
$Na^+ + 0.5Ca - X_2 \rightleftarrows 0.5Ca^{2+} + Na - X$	0.292 (0.282)
$Na^+ + 0.5Mg - X_2 \rightleftarrows 0.5Mg^{2+} + Na - X$	0.280 (0.344)
$Na^+ + K - X \rightleftarrows K^+ + Na - X$	0.138 (0.091)
$Na^+ + 0.5Fe - X_2 \rightleftarrows 0.5Fe^{2+} + Na - X$	0.5
Surface complexation	**Log K_{int}**
$\equiv S^SOH_2^+ \rightleftarrows \equiv S^SOH + H^+$	-4.5
$\equiv S^SO^- + H^+ \rightleftarrows \equiv S^SOH$	7.9
$\equiv S^SOFe^+ + H^+ \rightleftarrows \equiv S^SOH + Fe^{2+}$	0.6
$\equiv S^SOFeOH + 2H^+ \rightleftarrows \equiv S^SOH + Fe^{2+} + H_2O$	10.0

$\equiv S^{S}OFe(OH)_2^- + 3H^+ \rightleftarrows \equiv S^{S}OH + Fe^{2+} + 2H_2O$	20.0
$\equiv S^{W1}OH_2^+ \rightleftarrows \equiv S^{W1}OH + H^+$	-4.5
$\equiv S^{W1}O^- + H^+ \rightleftarrows \equiv S^{W1}OH$	7.9
$\equiv S^{W1}OFe^+ + H^+ \rightleftarrows \equiv S^{W1}OH + Fe^{2+}$	3.3
$\equiv S^{W2}OH_2^+ \rightleftarrows \equiv S^{W2}OH + H^+$	-6.0
$\equiv S^{W2}O^- + H^+ \rightleftarrows \equiv S^{W2}OH$	10.5

Table 2. Chemical composition of the granite boundary water and the initial bentonite porewater, which is equilibrated with the mineral phases (Samper *et al.*, 2008a).

Species	**Bentonite porewater after equilibration**	**Granite boundary water**
pH	6.46	7.825
Eh (V)	-0.078	-0.188
Ca^{2+} (mol/L)	$3.32 \cdot 10^{-2}$	$1.522 \cdot 10^{-4}$
Mg^{2+} (mol/L)	$3.67 \cdot 10^{-2}$	$1.604 \cdot 10^{-4}$
Na^{+} (mol/L)	$1.88 \cdot 10^{-1}$	$4.350 \cdot 10^{-3}$
K^{+} (mol/L)	$1.55 \cdot 10^{-3}$	$5.371 \cdot 10^{-5}$
Fe^{2+} (mol/L)	$1.43 \cdot 10^{-4}$	$1.791 \cdot 10^{-8}$
Cl^{-} (mol/L)	$2.75 \cdot 10^{-1}$	$3.949 \cdot 10^{-4}$
HCO_3^{-} (mol/L)	$7.59 \cdot 10^{-3}$	$5.049 \cdot 10^{-3}$
SO_4^{2-} (mol/L)	$2.05 \cdot 10^{-2}$	$1.561 \cdot 10^{-5}$
SiO_2 (aq) (mol/L)	$9.67 \cdot 10^{-5}$	$3.761 \cdot 10^{-4}$